

# Thermal conductivity of SiC microwires: Effect of temperature and structural domain size uncovered by 0 K limit phonon scattering

Bowen Zhu<sup>a</sup>, Ridong Wang<sup>a</sup>, Shay Harrison<sup>b</sup>, Kirk Williams<sup>b</sup>, Ram Goduguchinta<sup>b</sup>, John Schneider<sup>b</sup>, Joseph Pegna<sup>b</sup>, Erik Vaaler<sup>b</sup>, Xinwei Wang<sup>a,\*</sup>

<sup>a</sup> Department of Mechanical Engineering, Iowa State University, Ames, IA 50011, United States

<sup>b</sup> Free Form Fibers LLC., 10 Cady Hill Boulevard, Saratoga Springs, NY 12866, United States



## ARTICLE INFO

### Keywords:

Thermal conductivity  
Specific heat  
SiC microwires  
Grain size  
Spectroscopy

## ABSTRACT

A comparative study of structure and thermal properties is reported for three 3C crystalline silicon carbide (SiC) microwires, including Sylramic, Hi-Nicalon S and a sample fabricated by laser chemical vapor deposition (LCVD). Structural characterization by Raman spectroscopy and x-ray diffraction (XRD) finds that the LCVD-based sample contains excessive silicon and smallest grains of SiC but detectable free carbon. Thermal characterization from room temperature down to 20 K uncovers the effect of nanosized grain on thermal properties. The thermal properties are correlated with the structure via structural thermal domain (STD) size, defined as the grain boundary-induced phonon mean free path at the 0 K limit. The STD size of the three samples is found as 9.35, 1.42 and 1.03 nm for the Sylramic, Hi-Nicalon S and LCVD SiC fibers, proportional to and nearly one order of magnification smaller than the corresponding crystalline size determined by XRD: 67–113, 14.6–18.4, and 5.85–7.84 nm.

## 1. Introduction

Silicon carbide (SiC) microwires have been under active development in recent three decades as high-temperature materials for use in advanced gas turbine and nuclear fusion reactor. Since the introduction of the polymer-based technique first by Yajima et al. in 1970s, the as-fabricated SiC microwires have been commercialized and reached its state of the art [1]. The polymer-based SiC microwire exhibits high Young's modulus, high hardness, high thermal conductivity and a high resistance to creep, oxidation and thermal shock [2]. The fine diameter of about 10  $\mu\text{m}$  allows the microwires to be woven into and reinforce complex structures, typically in the form of ceramic matrix composites (CMC). In applications, the thermal conductivity of individual SiC microwires is of interest due to their fundamental role in the heat dissipation of the entire CMC component. However, previous study has been limited to the thermal characterization of CMC films instead of individual microwires [3], which further limits the understanding and improvement of SiC-based CMC. The challenge of accurate thermal characterization of individual microwires is mainly due to the specimen shape and size, which makes many techniques such as laser flash technique not applicable. Also the large surface-area-to-volume ratio significantly amplifies the radiation heat loss in thermal characterization. Typical steady-state techniques that extract thermal

properties from spatial temperature difference at a steady state are prone to the radiation effect [4]. In response, transient thermal techniques have been developed in the recent two decades for the measurement of microwires. The transient techniques that extract thermal properties from the transient temperature change (usually averaged in space) include time-domain thermoreflectance (TDTR) [5], 3- $\omega$  [6] and transient electro-thermal (TET) technique [7]. The TET technique that features no requirement for calibration and short data collection time is used in this work.

The objective of this work is to conduct a comparative study on the thermal properties and the microstructures of a series of advanced SiC microwires to provide the first-hand insight into the structure and thermal properties of nanocrystalline SiC, and to uncover the effect of structure on thermal transport capacity. Samples include Sylramic and Hi-Nicalon S fabricated by conversion of polymer precursors and LCVD-FFF fabricated by laser-driven chemical vapor deposition (LCVD) [8,9]. Their structure is characterized by x-ray diffraction (XRD) and Raman spectroscopy. The grain size determined by XRD ( $l_{\text{XRD}}$ ) is about 95, 16 and 7 nm for Sylramic, Hi-Nicalon S and LCVD-FFF, respectively. Thermal properties, including thermal conductivity ( $k$ ), thermal diffusivity ( $\alpha$ ) and volumetric heat capacity ( $\rho c_p$ ), are measured in the temperature range from room temperature (290 K) down to 20 K. Based on the measured thermal properties and grain size, the correlation

\* Corresponding author.

E-mail address: [xwang3@iastate.edu](mailto:xwang3@iastate.edu) (X. Wang).

between thermal properties and grain size is investigated and interpreted by the phonon scattering model. In contrast to the dominance of Umklapp phonon-phonon scattering in single crystals, grain boundary effect is overwhelming for the nanocrystalline samples. The structural thermal domain (STD) size, defined as the grain boundary-induced phonon mean free path (MFP) at 0 K limit, is found positively correlated to  $l_{\text{XRD}}$ .

## 2. Material and methods

### 2.1. Samples

The samples measured in this study include three 3C-SiC nanocrystalline microfibers: Sylramic, Hi-Nicalon S and LCVD-FFF. Sylramic (developed by Dow Corning and manufactured by COI Ceramics) is fabricated by the conversion of polytitanocarbosilane (PTC) precursor followed by pyrolysis in hydrogen with boron as additive [10]. Hi-Nicalon S (from Nippon Carbon) is fabricated by electron-beam curing of polycarbosilane (PCS) precursor followed by pyrolysis in hydrogen gas [9]. Both polymer-based fibers feature dominant 3C-SiC phase, near-stoichiometric composition (Si/C at% = 0.95–1, excessive carbon in the core) [11], low oxygen content (< 1 wt%) and low porosity [12]. The drawback of the polymer-based technique at the current stage is that the as-produced SiC microfibers have not been cost efficient and contain free carbon in the core or residual of additives [10,12,13]. LCVD-FFF from Free Form Fiber is fabricated by the LCVD process. In general, the growth of the core-less microwire is initiated by a laser beam, which provides the energy to break apart gas precursors and leads to the gas-phase reaction to form solid deposit, on a substrate that is mechanically pulled away from the deposition zone, thus producing long continuous fibers. The LCVD-based fiber features reduced fabrication cost and high purity of the fiber core, but has excessive silicon near periphery (a characteristic of CVD process for SiC [14]) and reduced grain size, which will be discussed in Section 3.1.

### 2.2. XRD characterization

XRD (Cu-K $\alpha$  source,  $\lambda = 0.15418$  nm) spectra were recorded by a Bruker D8 Advance diffractometer for a sample fiber bundle that had been attached to a zero-background holder with Vaseline. The incident beam is parallel with the fibers.

### 2.3. Raman spectroscopy

Raman spectroscopy was performed at room temperature using a confocal Raman system with back-scattering configuration. A green laser ( $\lambda = 532$  nm) beam was focused on the center of the cross section of the sample fiber. The focal spot size was restricted to 2.5  $\mu\text{m}$  in full width at half maximum by passing the incident beam through a 20  $\times$  lens. The laser power on the sample is estimated to be 7 mW for LCVD-FFF and 20 mW for the remained two. Raman signal was collected with an integration time of 10 s for LCVD-FFF and 4 s for the remained two.

### 2.4. Thermal characterization

Thermal characterization was performed in a close-cycle cryostat (Janis CCS-450) in vacuum (0.4–0.6 mTorr) using the TET technique. The measurement generally proceeds by applying a step current through an electrically conductive sample or a metallic coating that has been deposited on an electrically insulating sample. Since the three SiC samples display electrical insulation, 20-nm-thick iridium has been deposited on each sample by sputtering coating (Quorum 150 T S). The iridium coating serves both as a heater and a temperature sensor during measurement. The cryogenic TET configuration is shown in Fig. 1a. The sample fiber is suspended, with both ends covered by silver paste, over

a gap (1–2 mm) between two electrodes. The electrodes are connected to one another via alumina screws and thin mica layers. The sample holder composed of three aluminum electrodes is attached to a cold head with thermal grease. The temperature of the cold head is controlled by a monitoring/control unit (Lakeshore 335). Radiation heat loss is suppressed by shielding and convection by operating in a vacuum and reducing sample length (1–1.5 mm). During measurement, the Joule heating induced by the step current through the coating results in the temperature rise of the sample. The electrical resistance ( $R$ ) of iridium coating (Fig. 1b) is temperature dependent and can be depicted by the Bloch-Grüneisen formula [15]. Therefore, the temperature rise can be reflected by the voltage response (Fig. 1c) that rises with exponential decay. The heat transfer equation of the system can be simplified as a one-dimensional case due to the large aspect ratio ( $L/D > 30$ ,  $L$ : sample length,  $D$ : sample diameter) of microwire samples. The governing equation regardless of thermal radiation is written as

$$\frac{\rho c_p \partial T}{\partial t} = k \frac{\partial^2 T}{\partial x^2} + \dot{q}, \quad (1)$$

where  $\dot{q}$  is the electrical heating power per unit volume of the sample. The initial condition of the problem is  $T(x, t = 0) = T_0$ , where  $T_0$  is the initial temperature of the sample. The boundary condition is  $T(x = 0, t) = T(x = L, t) = T_0$  due to the bulk electrodes being as heat reservoirs. By assuming a linear  $R$ - $T$  correlation ( $dR/dT$  is actually nearly constant as seen in Fig. 1b) within the limited temperature rise ( $\Delta T$ , usually < 4 K) of each measurement, Eq. (1) can be solved analytically and the normalized voltage rise [ $V^*(t) = (V^t - V_0)/(V_\infty - V_0)$ ] mimics the normalized temperature [ $T^*(t) = (T^t - T_0)/(T_\infty - T_0)$ ], where  $V_0$  is the initial voltage,  $V_\infty$  and  $T_\infty$  are the voltage and temperature at steady state, respectively. The solution can be written as:

$$V^*(t) = T^*(t) = \frac{96}{\pi} \sum_{m=1}^{\infty} \frac{1 - \exp[-(2m-1)^2 \pi^2 \alpha_{\text{eff}} t / L^2]}{(2m-1)^4}, \quad (2)$$

where  $\alpha_{\text{eff}}$  is effective value that contains the radiation and coating effect. By fitting  $V^*(t)$ ,  $\alpha_{\text{eff}}$ , the only unknown parameter in Eq. (2) is obtained. The intrinsic  $\alpha$  is obtained by subtracting the contribution of radiation and the Ir coating, which has been detailed elsewhere [16]. Here, we provide the expression of the solution:

$$\alpha = \alpha_{\text{eff}} - \frac{16\epsilon\sigma T^3 L^2}{\pi^2 D \rho c_p} - \frac{L_{\text{Lorenz}} T L}{R A \rho c_p}, \quad (3)$$

where  $\epsilon$  is the surface emissivity,  $\sigma$  is the Stefan-Boltzmann constant,  $L_{\text{Lorenz}}$  is the Lorenz number, and  $A$  is the cross-sectional area of the sample.  $\epsilon$  is estimated as the average of  $\epsilon$  of SiC (0.9) and  $\epsilon$  of iridium coating (0.3) since about half of a fiber has been coated with iridium.  $L_{\text{Lorenz}}$  takes the Sommerfeld value ( $2.44 \times 10^{-8} \text{ W } \Omega/\text{K}^2$ ) in the temperature range of 20–290 K according to the previous research on  $L_{\text{Lorenz}}$  of sputtered iridium coating [17]. For the three samples in this study, the contribution of radiation and coating effect is evaluated to be less than 2%.

The effective thermal conductivity ( $k_{\text{eff}}$ ) is obtained from the particular solution at steady state ( $t = \infty$ ) in comparison with the initial state ( $t = 0$ ). It is expressed as

$$k_{\text{eff}} = \frac{I^2 R L}{12 A \Delta T}, \quad (4)$$

$\Delta T$  is given by the steady-state voltage rise and the  $R$ - $T$  correlation. The similarity of  $\rho c_p$  of iridium and SiC and the equivalent contribution of radiation to  $k_{\text{eff}}$  and  $\alpha_{\text{eff}}$  yield  $\rho c_p = k_{\text{eff}}/\alpha_{\text{eff}}$ . Hence,  $k = a \rho c_p$ . More details about the thermal process in TET characterization can be found in the work by Guo et al. [7]

The result of thermal characterization will be presented as the temperature dependence of  $k$  and  $\rho c_p$ .  $a$  will be presented as its inverse, thermal refusivity ( $\Theta$ ), for the interpretation of phonon scatterings. The uncertainty of  $a$  takes into account the voltage signal noise and the

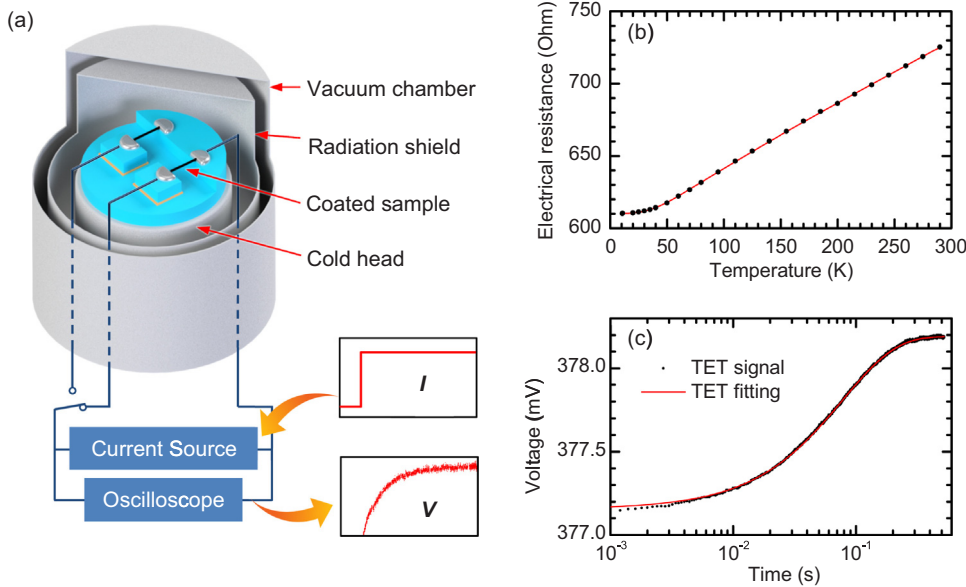


**Fig. 1.** Configuration and data processing of TET experiment. **(a)** Set-up of a cryogenic TET system. In a vacuum chamber (0.4–0.7 mTorr) with radiation shield, two microwire samples are suspended between aluminum electrodes. Both ends of a sample are covered by silver paste. The electrodes are electrically insulated from each other by thin mica layers and connected by ceramic screws. The current source provides a step current input. The oscilloscope monitors the voltage response in time domain. The aluminum electrodes are placed on the cold head of cryostat. **(b)** Temperature dependence of electrical resistance of the 20-nm iridium coating on the LCVD-FFF sample. The black dots are the measured data and the red line is the fitting curve of Bloch-Grüneisen formula. **(c)** TET voltage signal in logarithmic time domain. The voltage signal is a response to a 0.52-mA step current input during measurement of the LCVD-FFF sample (1495  $\mu\text{m}$  long and 34.3  $\mu\text{m}$  thick) at 290 K.

error of  $L$ . The uncertainty of  $k$  further includes the error of  $R$ - $T$  correlation and  $D$ . The uncertainty of  $\rho_{\text{c}}$  is induced by that of  $\alpha$  and  $k$ .

Let the measurement of LCVD-FFF be an example of data processing. The sample is 1495- $\mu\text{m}$  long, 34.29- $\mu\text{m}$  thick and coated with 20-nm Ir layer. The  $V$ - $t$  signal in Fig. 1b is the voltage response when a step current of 0.52 mA passes through the coating. By fitting the normalized  $V$ - $t$  signal with Eq. (2),  $\alpha_{\text{eff}} = 2.89 \text{ mm}^2$  is obtained. Using Eq. (3), the contribution of radiation effect and iridium coating effect is evaluated to be 1.6% and 0.3%, respectively. After subtracting both effects, we have  $\alpha = 2.83 \text{ mm}^2$ . The steady-state voltage rise  $\Delta V = 1.045 \text{ mV}$  in Fig. 1c can be translated to  $\Delta T = 4.74 \text{ K}$ , according to the  $R$ - $T$  dependence in Fig. 1b. Eq. (4) produces  $k_{\text{eff}} = 5.59 \text{ W/mK}$  and then  $\rho_{\text{c}} = k_{\text{eff}}/\alpha_{\text{eff}} = 1.94 \times 10^6 \text{ J/m}^3 \text{ K}$ . Finally, we have  $k = \alpha\rho_{\text{c}} = 5.49 \text{ W/mK}$ .

### 3. Results and discussion

#### 3.1. Structure analysis

The XRD results are shown in Fig. 2. The diffraction intensity versus diffraction angle ( $2\theta$ ) confirms that the main phase of the samples is 3C-SiC, indicated by the (111) peak ( $d = 0.251 \text{ nm}$ ,  $2\theta = 35.7^\circ$ ), (220) peak ( $d = 0.154 \text{ nm}$ ,  $2\theta = 60^\circ$ ) and (311) peak ( $d = 0.131 \text{ nm}$ ,  $2\theta = 71.8^\circ$ ).  $l_{\text{XRD}}$  is 67–114, 14–19 and 6–8 nm for Sylramic, Hi-Nicalon S and LCVD-FFF, respectively, using Scherrer equation, consistent with previous measurement of Sylramic and Hi-Nicalon S by both XRD and transmission electron microscope [10,18]. The specific  $l_{\text{XRD}}$  values for different  $2\theta$  are shown in Table 1. It is seen the grains in Hi-Nicalon S and LCVD-FFF SiC fibers have a low aspect ratio in its geometry, and the grain in Sylramic SiC fibers are shorter in the (111) direction, suggesting an oval shape. Note that the instrumental broadening ( $\beta_{\text{ins}}$ ) has been estimated as a constant  $0.07^\circ$ , which could result in an underestimation of  $\beta_{\text{ins}}$  for the (311) peak. Besides the SiC peaks, the presence of substantial titanium diboride ( $\text{TiB}_2$ ) and trivial titanium carbide (TiC) in Sylramic is assigned to the titanium precursor additive and boron sintering additive [10]. The unknown phase ( $2\theta = 31^\circ$ ) in Hi-Nicalon S is possibly related to fine quartz [19,20], considering the oxygen content has been found by Auger electron spectroscopy [11]. For LCVD-FFF, the silicon peaks are related to the excessive silicon content due to CVD processing. Quantitative phase analysis for LCVD-FFF presents 92.7 wt% of 3C-SiC, 5.3 wt% of Si and 2 wt% of unknown phase ( $2\theta = 29.6^\circ$ ).

The collected Raman spectra are presented in Fig. 3. In the region of

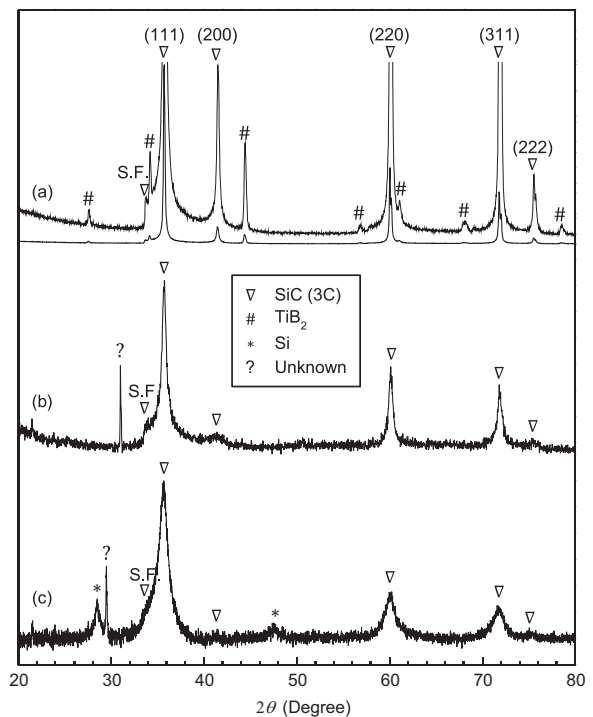


**Fig. 2.** XRD patterns of Sylramic **(a)**, Hi-Nicalon S **(b)** and LCVD-FFF **(c)**. An offset and enlarged view is provided for Sylramic. The sharp peaks besides (with less than half degree shift) the (220) and (311) peaks of SiC in Sylramic could be related to titanium carbide [37]. S.F. denotes stacking faults in 3C-SiC [38]. The baseline of **(c)** has been subtracted.

**Table 1**

Geometrical parameters and physical data extracted from the measurements of the three SiC microwire samples.

|              | $L$ ( $\mu\text{m}$ ) | $D$ ( $\mu\text{m}$ ) | $k_{\text{RT}}^*$ (W/mK) | $\Theta_0$ (s/cm <sup>2</sup> ) | $l_b$ (nm) | $l_{\text{XRD}}$ (nm) |       |       |
|--------------|-----------------------|-----------------------|--------------------------|---------------------------------|------------|-----------------------|-------|-------|
|              |                       |                       |                          |                                 |            | (111)                 | (220) | (311) |
| Sylramic     | 1060                  | 11.1                  | 46.3                     | 0.274                           | 9.35       | 66.8                  | 113   | 105   |
| Hi-Nicalon S | 1193                  | 9.0                   | 21.7                     | 1.807                           | 1.42       | 14.6                  | 18.4  | 15.7  |
| LCVD-FFF     | 1495                  | 34.3                  | 5.5                      | 2.483                           | 1.03       | 7.84                  | 7.47  | 5.85  |

\*  $k_{\text{RT}}$  denotes the thermal conductivity at room temperature (290 K).

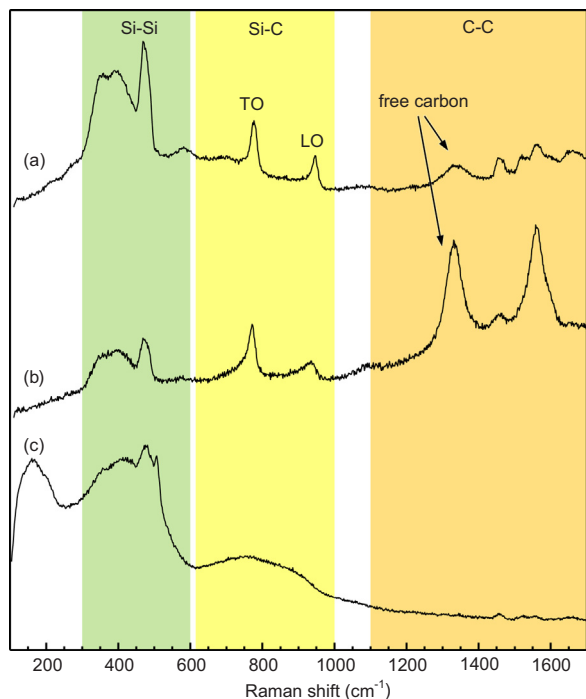


Fig. 3. Raman spectra obtained at the core of Sylramic (a), Hi-Nicalon S (b) and LCVD-FFF (c). The peaks for Si-Si, Si-C and C-C vibration modes are located in the range of 300–600, 600–1000 and 1100–1700  $\text{cm}^{-1}$ , respectively.

carbon bands between 1100 and 1600  $\text{cm}^{-1}$ , two peaks at 1350 and 1560  $\text{cm}^{-1}$  (Fig. 3a-b) are found for Sylramic and Hi-Nicalon S. The former peak is generally assigned to free carbon while the latter corresponds to graphite [21]. This implies a considerable amount of free carbon in the core. The Raman peaks for Si-C bond vibration are generally located in the region between 600 and 1000  $\text{cm}^{-1}$ . The transverse optical (TO) phonon band and longitudinal optical (LO) phonon band of 3C-SiC single crystals are expected to be present at 796  $\text{cm}^{-1}$  and at 972  $\text{cm}^{-1}$ , respectively. For Sylramic and Hi-Nicalon S, the two bands are displaced from their nominal position, shifting to lower frequency with increased width due to the nanosized grains. It has been reported that both the peak shift and the peak width are proportional to the inverse of grain size [22,23], and also influenced by stacking faults [24]. Therefore, quantitative analysis is not plausible here. Despite this, it can be observed that the two Si-C peaks of Sylramic is sharper and has less shifting than Hi-Nicalon S, agreeing with the observation of  $l_{\text{XRD}}$ . In the spectrum of LCVD-FFF, only a broad peak can be found in the same region of Raman shift. It is probably due to the small grain size ( $l_{\text{XRD}} = \sim 7 \text{ nm}$ ), which heavily disturbs the vibration of Si-C bonds in crystallites.

### 3.2. Thermal conductivity and specific heat

The scanning electron microscope (SEM) images of the samples for thermal characterization are shown in Fig. 4. For Sylramic, Hi-Nicalon S and LCVD-FFF, the length is 1060, 1193 and 1495  $\mu\text{m}$ , and the diameter is 11.1, 9.0 and 34.3  $\mu\text{m}$ , respectively. The temperature dependence of thermal conductivity of the three samples is presented in Fig. 5a. Compared with single crystal and polycrystalline bulk samples of larger grain size from literature [13,25], the nanocrystalline microwire samples possess lower thermal conductivities in general and higher characteristic temperatures where thermal conductivity maximizes. The tendency has also been observed for other nanocrystalline structures [26–29]. We attribute the difference in thermal conductivity to the introduction of grain boundaries. The role of grain size in temperature dependence of thermal conductivity can be illustrated qualitatively in

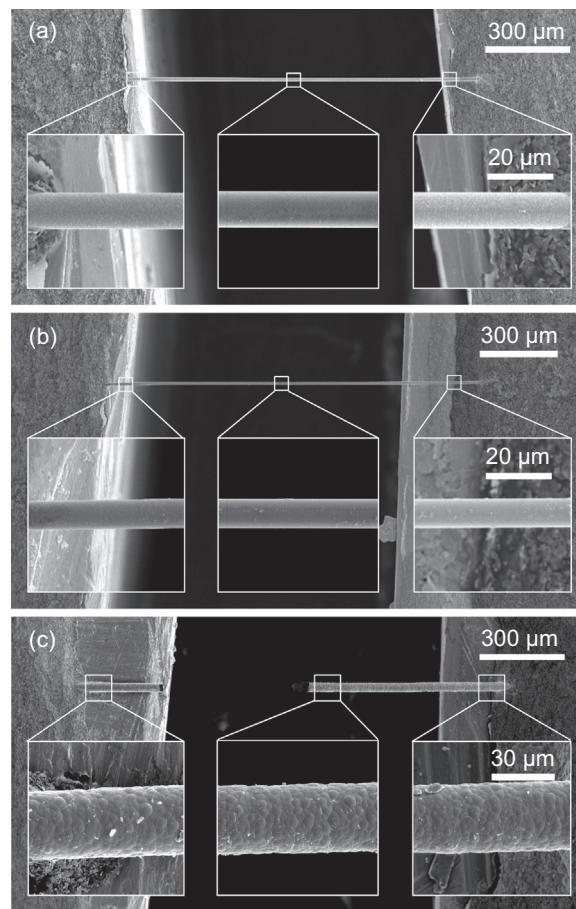
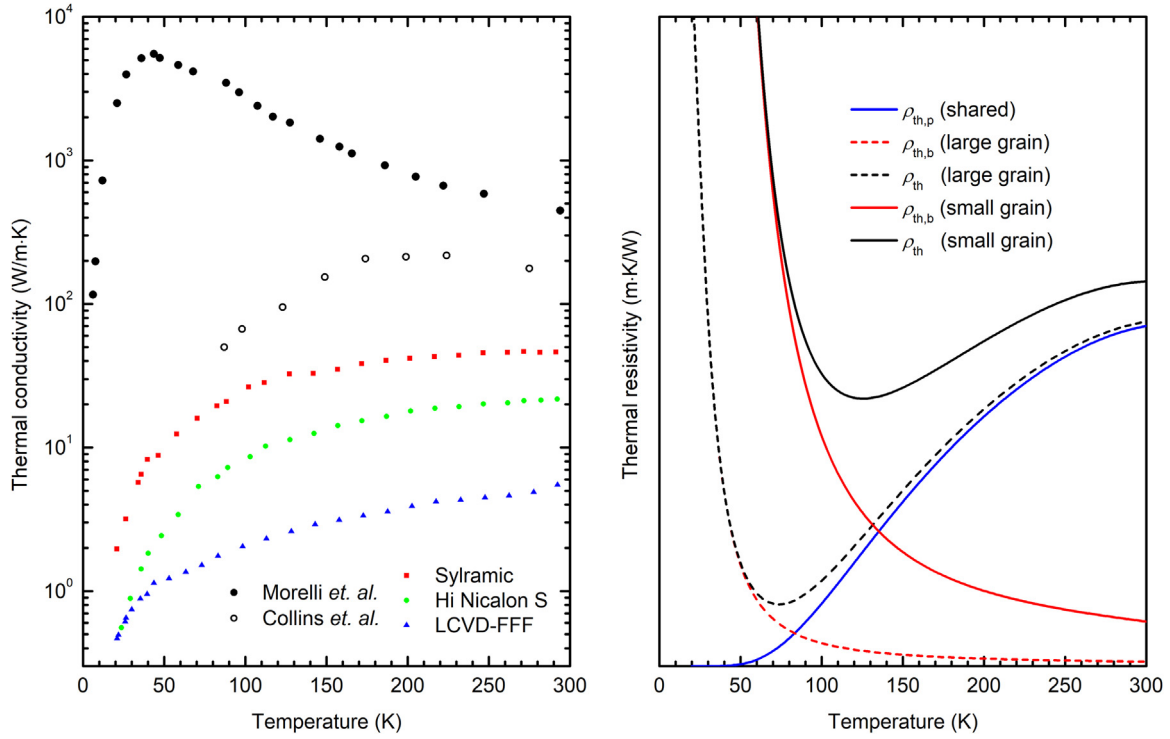


Fig. 4. SEM images of Sylramic (a), Hi-Nicalon S (b) and LCVD-FFF (c) prepared for TET experiment. For each sample, an overview and three insets are given for showing the length and diameter, respectively. The LCVD-FFF was broken accidentally after thermal characterization.

the frame of single-relaxation-time approximation. For brevity of expression, thermal resistivity  $\rho_{\text{th}} \equiv k^{-1}$  is employed instead of  $k$ . The thermal resistivity of SiC of finite grain size can be expressed by  $\rho_{\text{th}} = 3/\rho_{\text{c}}v_l$ , where  $l$  and  $v$  are phonon mean free path and phonon group velocity, respectively [30,31]. The phonon mean free path is constrained by phonon scatterings induced by Umklapp process  $l_{\text{p}}$  and grain boundaries  $l_{\text{b}}$ . By assuming the independence of different scattering effects, Matthiessen's rule gives  $l^{-1} = l_{\text{p}}^{-1} + l_{\text{b}}^{-1}$ . Here,  $l_{\text{b}}$  is insensitive to temperature while, at low temperatures,  $l_{\text{p}}^{-1}$  is proportional to the temperature dependent Boltzmann's factor  $e^{-T_{\text{D}}/2T}$  [32,33], where  $T_{\text{D}}$  is Debye temperature. In this way, the thermal resistivity  $\rho_{\text{th}}$  can be decomposed into two fractions, the Umklapp thermal resistivity  $\rho_{\text{th,p}} = 3/\rho_{\text{c}}v_l C e^{-T_{\text{D}}/2T}$  ( $C$  is a constant) and the grain boundary-induced thermal resistivity  $\rho_{\text{th,b}} = 3/\rho_{\text{c}}v_l l_{\text{b}}$ . The temperature dependence of the two fractions and their sum is sketched in Fig. 5b for samples of large grain size (denoted by dash line) and small grain size (denoted by solid line). Here we assume  $\rho_{\text{th,b}}$  is independent of grain size and  $\rho_{\text{c}}$  obeys Debye's approximation [33]. For the sample of reduced grain size,  $l_{\text{b}}^{-1}$  is increased and  $\rho_{\text{th,b}}$  is therefore proportionally amplified. Consequently, for small-grain sample,  $\rho_{\text{th}}$  is larger and the minimum of  $\rho_{\text{th}}$  is located at a higher temperature. The corresponding thermal conductivity will decrease and maximize at a higher temperature as grain size decreases.

Shown in Fig. 6 is the measured volumetric heat capacity.  $\rho_{\text{c}}$  of the three samples does not significantly deviate from one another, consistent with Debye's approximation for low-frequency phonons [33]. Their  $\rho_{\text{c}}$  is proportional to  $T$  as  $T > 100 \text{ K}$ , while the order of temperature dependence is between 2 and 3 as  $T < 50 \text{ K}$ .



**Fig. 5.** (a) Thermal conductivity of Syramic, Hi-Nicalon S and LCVD-FFF, plotted in semi-log scale. Also shown is the thermal conductivity of SiC single crystal bulk (1-mm grain size) measured by Morelli et al., [25] and SiC polycrystalline bulk (17- $\mu$ m grain size) by Collins et al. [13] (b) Variation of Umklapp thermal resistivity  $\rho_{th,p}$ , grain boundary-induced thermal resistivity  $\rho_{th,b}$  and their sum  $\rho_{th}$  versus temperature for samples of large grain size and small grain size.  $\rho_{th,p}$  is assumed the same for both cases and is therefore denoted as “shared”.

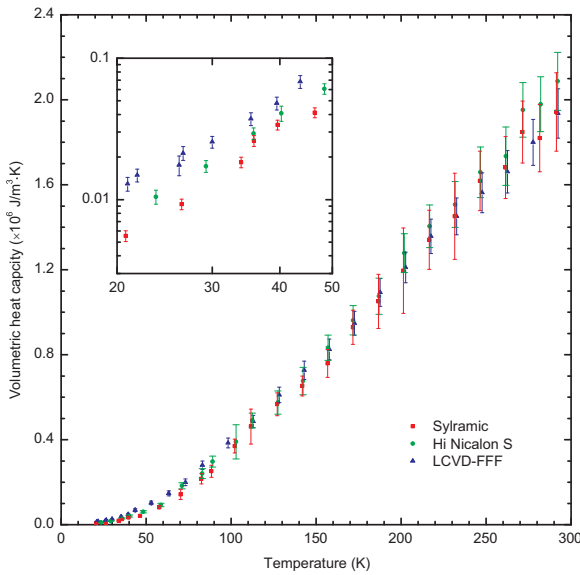


**Fig. 6.** Volumetric heat capacity of Syramic, Hi-Nicalon S and LCVD-FFF. The inset is the volumetric heat capacity between 20 and 50 K, plotted in log-log scale.

### 3.3. Structural domain size

For the investigation of the correlation between structure and thermal properties, the effect of  $\rho_{cp}$ , which is temperature dependent and cannot be measured with sound accuracy, should be ruled out. Hence we will study the correlation between the directly measured thermal reffusivity  $\Theta \equiv 1/\alpha$  and phonon mean free path [17]. Based on the single-relaxation time approximation,  $\Theta$  can be expressed by

$$\Theta = \frac{1}{3v} \left( \frac{1}{l_p} + \frac{1}{l_b} \right) = Ce^{-T_D/2T} + \frac{1}{3vl_b}, \quad (5)$$

$v$  in the Umklapp term  $Ce^{-T_D/2T}$  merges into the constant  $C$  as  $v$  of acoustic phonon modes is independent of temperature (i.e.  $v = 12600\text{--}13300$  m/s for  $T = 5\text{--}300$  K) and optical phonons are negligible [34]. As  $T \rightarrow 0$ , the Umklapp scattering is inhibited ( $Ce^{-T_D/2T} \rightarrow 0$ ) while the grain boundary-induced term, defined as  $\Theta_0 = 1/3vl_b$ , remains.  $v$  in this work is taken as 13000 m/s. In this way, the directly measured thermal property  $\Theta$  is associated with the structure-induced property  $l_b$ . Here,  $l_b$  is termed “Structure Thermal Domain” (STD) size as it is determined by the thermal transport and solely induced by the structure.

As seen in Fig. 7, the  $\Theta$ - $T$  data generally follows the model of Eq. (5) when temperature is sufficiently low.  $T_D$  of the three samples is significantly lower than that of 3C-SiC bulk (1000–1300 K) [35] and falls in the range of 220–290 K, suggesting the confinement of high-frequency vibration modes by the nanocrystalline structure. The discrepancy of fitting at high temperature also suggests that some high-frequency modes are allowed for the two samples of larger grain size. The high frequency terms are not added into the formula for the fitting at high temperatures since the discrepancy does not influence the parameters of interest:  $\Theta_0$  and STD size. The intercept of the fitting curves  $\Theta_0$  is determined to be  $2742 \pm 75$ ,  $18066 \pm 481$  and  $24834 \pm 1080$  s/m<sup>2</sup>, and the STD size is  $9.35 \pm 0.56$ ,  $1.42 \pm 0.08$  and  $1.03 \pm 0.07$  nm for Syramic, Hi-Nicalon S and LCVD-FFF, respectively. The results are summarized in Table 1 and compared with the grain size determined by XRD. We find that STD size is approximately proportional to the grain size. Probably because the STD size and  $l_{XRD}$  are related to the scattering effect induced by the same material structure although the former is associated with phonons and the latter is with x-ray photons. In addition, the STD size is about an order of magnitude smaller than  $l_{XRD}$ . A possible reason is that the broadening of XRD peak is related to the size of the ordered atoms in a certain

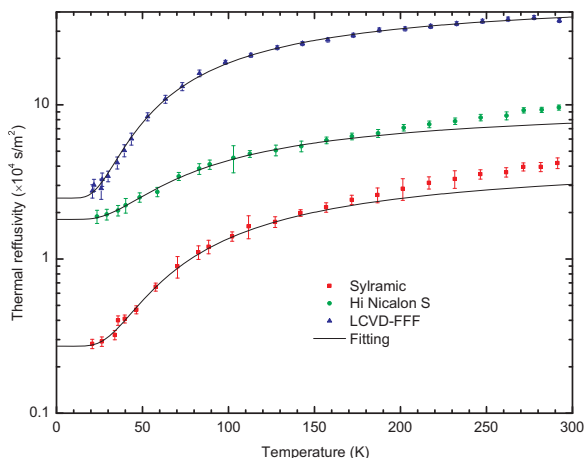


**Fig. 7.** Thermal reffusivity of Syramic, Hi-Nicalon S and LCVD-FFF, plotted in semi-log scale. The fitting function is  $\Theta = C \exp(-T_D/2T) + \Theta_0$ , where the constant  $C$ , Debye temperature  $T_D$  and residual thermal reffusivity  $\Theta_0$  are parameters being fitted. In the fitting, Syramic has  $\Theta_0 = 2720 \text{ m}^2/\text{s}$ ,  $C = 44503 \text{ m}^2/\text{s}$ ,  $T_D = 282 \text{ K}$ ; Hi-Nicalon S has  $\Theta_0 = 18066 \text{ m}^2/\text{s}$ ,  $C = 87283 \text{ m}^2/\text{s}$ ,  $T_D = 246 \text{ K}$ ; LCVD-FFF has  $\Theta_0 = 24834 \text{ m}^2/\text{s}$ ,  $C = 506598 \text{ m}^2/\text{s}$ ,  $T_D = 228 \text{ K}$ .

direction while the STD size can be confined by the disordered structure in all directions. More specifically, phonon propagation can be constrained by the grain boundaries that do not intersect the propagation path. Therefore, the STD size is smaller than the grain size. Also the much smaller STD size suggests rough grain boundaries that introduces extremely strong phonon scattering. It should be noted that the microstrain [36] and stacking faults [24] that can influence the phonon velocity and phonon lifetime are not taken into account in the modeling of phonon transport here. Despite this, the proportionality between STD size and  $l_{\text{XRD}}$  provides a very clear correlation between material structure and thermal properties.

#### 4. Conclusion

In summary, we have measured and compared the thermal properties of three advanced SiC microwires in the temperature range of 20–290 K. The room-temperature thermal conductivity of Syramic, Hi-Nicalon S and LCVD-FFF is 46.3, 21.7 and 5.5 W/m·K, respectively, much smaller than the bulk value. Due to the dominance of phonon-boundary scattering, the Umklapp thermal conductivity ( $\kappa \propto T^{-1}$ ) is not observable in the measured temperature range. The heat capacities obey the classic Debye model. The structural thermal domain size deduced from low-temperature thermal characterization is found to be comparable with the grain size determined by XRD. Specifically, for Syramic, Hi-Nicalon S and LCVD-FFF, the structural thermal domains were determined as 9.35, 1.42 and 1.03 nm, respectively, proportional to the grain sizes with a factor of 0.1. This finding provides a clear understanding of the correlation between grain size and thermal properties.

#### Acknowledgements

The authors thank Free Form Fibers for providing the samples. We also thank Steven Mercurio for his help and advice on the XRD analysis. XRD characterization was performed at Alfred University at Alfred, NY. Support of this work by National Science Foundation (CBET1235852, CMMI1264399), Department of Energy (DENE0000671), and Iowa Energy Center (OG-17-005) is gratefully acknowledged.

#### Declaration of interest

None.

#### References

- [1] S. Yajima, J. Hayashi, M. Omori, Continuous silicon carbide fiber of high tensile strength, *Chem. Lett.* 4 (1975) 931–934.
- [2] L. Rovner, G. Hopkins, Ceramic materials for fusion, *Nucl. Technol.* 29 (1976) 274–302.
- [3] T. Ishikawa, S. Kajii, K. Matsunaga, T. Hogami, Y. Kohtoku, T. Nagasawa, A. Tough, Thermally conductive silicon carbide composite with high strength up to 1600 °C in air, *Science* 282 (1998) 1295.
- [4] D.G. Cahill, R.O. Pohl, Thermal conductivity of amorphous solids above the plateau, *Phys. Rev. B* 35 (1987) 4067–4073.
- [5] X. Wang, V. Ho, R.A. Segalman, D.G. Cahill, Thermal conductivity of high-modulus polymer fibers, *Macromol* 46 (2013) 4937–4943.
- [6] L. Lu, W. Yi, D. Zhang,  $3\omega$  method for specific heat and thermal conductivity measurements, *Rev. Sci. Instrum.* 72 (2001) 2996–3003.
- [7] J. Guo, X. Wang, T. Wang, Thermal characterization of microscale conductive and nonconductive wires using transient electrothermal technique, *J. Appl. Phys.* 101 (2007) 063537.
- [8] H.M. Yun, J.A. DiCarlo, Comparison of the tensile, creep, and rupture strength properties of stoichiometric SiC fibers, *Ceram. Eng. Sci. Proc.* 20 (1999) 259–272.
- [9] M. Takeda, J. Sakamoto, A. Saeki, Y. Imai, H. Ichikawa, High-performance silicon carbide fiber Hi-Nicalon for ceramic matrix composites, *Ceram. Eng. Sci. Proc.* 16 (1995) 37–44.
- [10] A.R. Bunsell, M.H. Berger, Fine diameter ceramic fibres, *J. Eur. Ceram. Soc.* 20 (2000) 2249–2260.
- [11] S. Dong, G. Chollon, C. Labrugere, M. Lahaye, A. Guette, J. Bruneel, M. Couzi, R. Naslain, D. Jiang, Characterization of nearly stoichiometric SiC ceramic fibres, *J. Mater. Sci.* 36 (2001) 2371–2381.
- [12] J.A. DiCarlo, H.-M. Yun, Non-oxide (silicon carbide) fibers, in: N.P. Bansal (Ed.), *Handbook of Ceramic Composites*, Springer, US, Boston, MA, 2005, pp. 33–52.
- [13] A.K. Collins, M.A. Pickering, R.L. Taylor, Grain size dependence of the thermal conductivity of polycrystalline chemical vapor deposited  $\beta$ -SiC at low temperatures, *J. Appl. Phys.* 68 (1990) 6510–6512.
- [14] K. Minato, K. Fukuda, Structure of chemically vapour deposited silicon carbide for coated fuel particles, *J. Mater. Sci.* 23 (1988) 699–706.
- [15] J.M. Ziman, *Electrons and Phonons: The Theory of Transport Phenomena in Solids*, Clarendon, Oxford, 1960.
- [16] G. Liu, S. Xu, T. Cao, H. Lin, X. Tang, Y. Zhang, X. Wang, Thermally induced increase in energy transport capacity of silkworm silks, *Biopolymers* 101 (2014) 1029–1037.
- [17] Z. Xu, *Thermal Transport in DNA*, Mechanical Engineering, Iowa State University, Ames, 2015.
- [18] F. Solá, R. Bhatt, Mapping the local modulus of syramic silicon carbide fibers by nanoindentation, *Mater. Lett.* 159 (2015) 395–398.
- [19] P.J. Baxter, C. Bonadonna, R. Dupree, V.L. Hards, S.C. Kohn, M.D. Murphy, A. Nichols, R.A. Nicholson, G. Norton, A. Searl, R.S.J. Sparks, B.P. Vickers, Cristobalite in volcanic ash of the Soufriere Hills Volcano, Montserrat, *British West Indies, Science* 283 (1999) 1142–1145.
- [20] C. Elmi, J. Chen, D. Goldsby, R. Gieré, Mineralogical and compositional features of rock fulgurites: a record of lightning effects on granite, *Am. Mineral.* 102 (2017) 1470.
- [21] G. Chollon, R. Pailler, R. Naslain, F. Laanani, M. Monthieux, P. Olry, Thermal stability of a PCS-derived SiC fibre with a low oxygen content (Hi-Nicalon), *J. Mater. Sci.* 32 (1997) 327–347.
- [22] G. Gouadec, P. Colomban, Raman spectroscopy of nanomaterials: how spectra relate to disorder, particle size and mechanical properties, *Prog. Cryst. Growth Character Mater.* 53 (2007) 1–56.
- [23] R. Nemanich, S. Solin, R.M. Martin, Light scattering study of boron nitride microcrystals, *Phys. Rev. B* 23 (1981) 6348.
- [24] J. Lipowitz, J.A. Rabe, A. Zangvil, Y. Xu, Structure and properties of Syramic silicon carbide fiber—a polycrystalline, stoichiometric  $\beta$ -SiC composition, *Ceram. Eng. Sci. Proc.* 18 (1997) 147–157.
- [25] D.T. Morelli, J.P. Heremans, G.A. Slack, Estimation of the isotope effect on the lattice thermal conductivity of group IV and group III-V semiconductors, *Phys. Rev. B* 66 (2002) 195304.
- [26] D. Li, Y. Wu, P. Kim, L. Shi, P. Yang, A. Majumdar, Thermal conductivity of individual silicon nanowires, *Appl. Phys. Lett.* 83 (2003) 2934–2936.
- [27] N. Mingo, L. Yang, D. Li, A. Majumdar, Predicting the thermal conductivity of Si and Ge nanowires, *Nano Lett.* 3 (2003) 1713–1716.
- [28] R. Chen, A.I. Hochbaum, P. Murphy, J. Moore, P. Yang, A. Majumdar, Thermal conductance of thin silicon nanowires, *Phys. Rev. Lett.* 101 (2008) 105501.
- [29] Z. Wang, J.E. Alaniz, W. Jang, J.E. Garay, C. Dames, Thermal conductivity of nanocrystalline silicon: importance of grain size and frequency-dependent mean free paths, *Nano Lett.* 11 (2011) 2206–2213.
- [30] B.H. Armstrong, N processes, the relaxation-time approximation, and lattice thermal conductivity, *Phys. Rev. B* 32 (1985) 3381.
- [31] J. Callaway, Model for lattice thermal conductivity at low temperatures, *Phys. Rev.* 113 (1959) 1046–1051.
- [32] Y. Xie, Z. Xu, S. Xu, Z. Cheng, N. Hashemi, C. Deng, X. Wang, The defect level and ideal thermal conductivity of graphene uncovered by residual thermal reffusivity at

- the 0 K limit, *Nanoscale* 7 (2015) 10101–10110.
- [33] C. Kittel, *Introduction to Solid State Physics*, 8th ed., John Wiley & Sons, New York, United States, 2005.
- [34] G.L. Harris, *Properties of Silicon Carbide*, INSPEC, the Institution of Electrical Engineers, London, 1995.
- [35] O. Madelung, U. Rössler, M. Schulz, *Semiconductors: Group IV Elements, IV–IV and III–IV Compounds*, Landolt-Börnstein, New Series, Group III, 41 Springer-Verlag, Berlin, 2005.
- [36] M. Fujii, Y. Kanzawa, S. Hayashi, K. Yamamoto, Raman scattering from acoustic phonons confined in Si nanocrystals, *Phys. Rev. B* 54 (1996) R8373.
- [37] H. Kaifu, H. Yemin, M. Yanwen, L. Yinong, H. Zheng, C. Yi, Synthesis and field emission properties of titanium carbide nanowires, *Nanotechnol* 18 (2007) 145615.
- [38] K. Koumoto, S. Takeda, C.H. Pai, T. Sato, H. Yanagida, High-resolution electron microscopy observations of stacking faults in  $\beta$ -SiC, *J. Am. Ceram. Soc.* 72 (1989) 1985–1987.